Importance of isovector effects in reproducing neutron total cross section differences in the W isotopes

F. S. Dietrich, J. D. Anderson, and R. W. Bauer
Lawrence Livermore National Laboratory, Livermore, California 94550

S. M. Grimes and R. W. Finlay
Ohio University, Athens, Ohio 45701

W. P. Abfalterer, F. B. Bateman,* R. C. Haight, and G. L. Morgan
Los Alamos National Laboratory, Los Alamos, New Mexico 87545

E. Bauge, J.-P. Delaroche, and P. Romain
CEA, Département de Physique Théorique Appliquée, Boîte Postale 12, F-91680 Bruyères-le-Châtel, France
(Received 11 October 2002; published 28 April 2003)

Cross section differences among the isotopes ^{182,184,186}W have been measured as a part of a study of total cross sections in the 5–560 MeV energy range. These difference measurements show oscillations up to 150 mb between 5 and 100 MeV. Calculations with spherical and deformed phenomenological optical potentials employing standard radial and isospin dependences show much smaller oscillations than the experimental data. In a simple Ramsauer model, this discrepancy can be traced to a cancellation between radial and isospin effects. Understanding this problem requires a more detailed model that incorporates a realistic description of the neutron and proton density distributions. This has been done with the results of Hartree-Fock-Bogoliubov calculations using the Gogny force, together with a microscopic folding model employing a modification of the Jeukenne, Lejeune, and Mahaux potential as an effective interaction. This treatment yields a satisfactory interpretation of the observed total cross section differences up to 200 MeV. The calculations have been extended above that energy with a folding model based on an empirical effective interaction.

DOI: 10.1103/PhysRevC.67.044606 PACS number(s): 28.20.Cz, 25.40.−h, 24.10.Ht

I. INTRODUCTION

Differences of neutron total cross sections among neighboring nuclei provide unusually stringent tests of optical models. In many cases, standard optical potentials with nuclear radii proportional to $A^{1/3}$ and with typical strengths for isovector components [$U_1/U_0 \approx 0.5$ in the usual expression $U = U_0 \pm U_1(N-Z)/A$] have yielded a reasonably good agreement with measured cross section differences. Examples may be found in the Ce region [1] and in the Nd-Sm region [2], as well as ^{238}U-^{232}Th [3]. The results in the Ce region have also been reproduced with a microscopic folding model [4].

In this work, we report on the new measurements of the total cross sections of the tungsten isotopes ^{182,184,186}W in the energy range 5–560 MeV, and we show that the standard optical model treatment fails to reproduce the observed differences of cross sections among these isotopes. The essential problem is that the effects of change of radius and change in the isospin terms approximately cancel, leading to weakly energy-dependent values for the cross section differences, whereas the measurements show distinct oscillations in the range 5–100 MeV.

To gain insight into this problem, we have employed a simple Ramsauer model that has proven successful in reproducing the energy dependence of total cross sections [5–7]. Whereas this model successfully reproduces cross section differences in the Ce region, it fails to reproduce the observed differences among the W isotopes. However, extending this model by adding the excess neutrons to the nuclear surface in calculating the differences between ^{186}W-^{182}W and ^{186}W-^{184}W improves the agreement with the experiment. This suggests that the origin of the observed differences lies in the surface behavior of the nucleus, and points to the need for including a realistic description of the nuclear surface in more detailed physical models.

The W isotopes are known to be reasonably well described as deformed rotors, and such deformations give rise to surface effects. We have used coupled-channel calculations to investigate the role of deformation in the cross section differences. These calculations were made with a phenomenological optical potential incorporating the dispersion relation relating the real and imaginary potentials. As is the case with spherical potentials, we find that these calculations, which employ standard radial and isospin dependences on A and N, do not adequately explain the observed cross section differences.

Hartree-Fock calculations describe neutron and proton density distributions separately, and they predict larger rms radii for neutrons than for protons in heavy nuclei. Thus they may also provide the surface effects required to address the experimental data. We have used such density distribu-

*Present address: National Institute of Standards and Technology, Gaithersburg, MD 20899.

tions from a Hartree-Fock-Bogoliubov calculation [8,9] in a microscopic folding model. This model uses an effective interaction [10] based on the JLM (Jeukenne, Lejeune, and Mahaux) optical potential [11,12] that has been adjusted to yield a Lane-consistent description [13] of nucleon scattering; that is, it adequately describes neutron and proton elastic scattering as well as (p,n) reactions to isobaric analog states over a wide mass and energy range. We have performed both spherical and coupled-channel calculations using this treatment. No additional parameter adjustment has been made. Both of these calculations adequately describe the observed total cross section differences.

The results of this work show that understanding total cross section differences between nearby nuclei requires careful attention to details of the nuclear density distributions. Simple models that do not take these details into account may fail, as in the case presented here. We have shown that a folding model based on realistic nuclear densities and an isospin-consistent effective interaction provide the necessary ingredients for addressing total cross section differences.

The paper is organized as follows. Section II describes the cross section difference measurements. Section III shows the analysis of the results using the Ramsauer and spherical phenomenological optical models; this is followed in Sec. IV by a description of the most complete phenomenological treatment available using dispersive optical potentials in a coupled-channel context. Section V describes the folding calculations, and the paper concludes with a short summary in Sec. VI.

II. EXPERIMENT

The neutron total cross sections of ^{182,184,186}W in the energy range 5–500 MeV were measured at the LANSCE/WNR facility at the Los Alamos National Laboratory as part of an extensive survey of total cross sections spanning the periodic table from A$A=1$ to 238. Nearly all of the results of these measurements have been published [14,15], and details of the experiment and the uncertainties are contained in these references and in a report [16]. The techniques employed were a refinement of those in an earlier survey [17] carried out at LANSCE/WNR. The measurements were made by the transmission method in which a well-collimated neutron beam is incident along the sample axis and the count rates in plastic-scintillator counters downstream of the samples were compared with the samples in and out of the beam. We note here only the experimental details that are specific to the measurements on the isotopic samples of ^{182,184,186}W.

The data in the main part of the experiment, which included a natural tungsten sample, were reported in 1% wide energy bins, with a statistical accuracy of 1% or better in each bin. To exhibit the cross section differences among the separated isotopes adequately, we have binned the data in 8% wide intervals, with a statistical accuracy of approximately 0.2% in each bin.

In principle, the data should be corrected for accidental coincidences in the charged-particle veto paddles placed in front of the main neutron detectors. This was done for the data reported in Ref. [14]. Sufficient information was not available to make these corrections for the separated-isotope data. Accordingly, we have restricted the upper limit of the energy range to 500 MeV, since the veto corrections significantly affect the data only above that energy.

The neutron beam was defined by iron collimators upstream and downstream of the samples. These collimators were of such sufficiently small diameter that neutrons could not reach the detector without passing through the samples. To ensure that this condition was satisfied for the isotopic tungsten samples, it was necessary to replace the approximately 1.9-cm inside-diameter collimators used for the majority of the measurements with a new set having an inside diameter of 1.27 cm [14,16].

The samples were mounted on a rotating wheel that allowed data to be taken in successive 20 sec intervals for each of the three tungsten samples and a sample-out position. As a control on systematic errors, the data were taken in three batches. The samples were interchanged between each batch. There was no indication of differing results among the three batches that exceeded statistical errors. Final results were obtained by averaging the partial results from each of the three batches.

The isotopic samples were cylinders of pressed sintered material approximately 2.1 cm in diameter and of approximately the same length (1.95–1.99 cm). These samples were apparently the same as used in previous measurements of total cross sections [18] and angular distributions [19]. Table I shows the isotopic composition for each sample as quoted by the supplier, the Isotope Distribution Office at Oak Ridge National Laboratory. The maximum contamination of tungsten isotopes other than the principal one is approximately 6%. We have not made corrections for these impurities.

The densities were determined by hand measurements (length, diameter, and weight), by a water immersion technique, and by measuring the attenuation of γ rays incident along the axis of the cylinders [16]. The hand measurements were difficult because the samples were not perfect right-circular cylinders and the surfaces had irregularities. Results for the bulk and areal densities from the water immersion technique are indicated in Table I. The inverse areal densities $(1/nl)$ shown in this table were used in the analysis of the data. The extracted cross sections are directly proportional to this quantity.

The densities determined by γ attenuation were lower than those from the water immersion method by approximately 2–4 %. We attribute part of this discrepancy to insufficient knowledge of the γ attenuation coefficient, since a well-characterized tantalum sample showed a deficiency of 1.8%. The important result is that the differences of the densities among the tungsten isotopes determined by the two methods are inconsistent. This suggests that the samples have internal voids or density gradients that may have arisen during the manufacturing process. This possibility is supported by the fact that the average density as measured by water immersion is approximately 6% lower than that for the natural tungsten sample used in the main part of the experiment [14].

The dots in Fig. 1 show an isotopically weighted average

TABLE I. Sintered tungsten isotopes. We believe that the same sample materials were used in Ref. [18] in the measurement of neutron total and scattering cross sections, and that the same ^{182,184}W samples were used in Ref. [19] in the measurement of direct neutron scattering cross sections. The isotopic abundances for ^{182}W and ^{184}W listed in Ref. [18] are slightly different from the ones quoted to us by the supplier (Isotope Distribution Office, Oak Ridge National Laboratory); namely, 94.9% instead of 93.86% for ^{182}W, and 98.88% instead of 94.00% for ^{184}W.

Sample name	Mass (g)	Length (cm)	Diameter[a] (cm)	Density (g/cm^3)	$1/nl$ (b/atom)	at. % (%)
^{182}W	124.36	1.949	2.108/2.129	18.282	8.480	^{182}W: 93.86, ^{183}W: 2.37 ^{184}W: 2.49, ^{186}W: 1.28
^{184}W	124.07	1.991	2.040/2.109	18.465	8.309	^{182}W: 1.46, ^{183}W: 1.62 ^{184}W: 94.00, ^{186}W: 2.92
^{186}W	123.11	1.984	2.023/2.099	18.655	8.343	^{182}W: 0.58, ^{183}W: 0.41 ^{184}W: 1.34, ^{186}W: 97.66

[a]Minimum/maximum diameter of the sample.

of the three cross sections [neglecting the small (14.4%) contributions of ^{180}W and ^{183}W], after an upward normalization by 2.2%. The energy dependence of the cross section is in excellent agreement with that measured for natural W, shown by the solid line in the figure. This upward normalization is another indication of the uncertainties in the sample densities. From this result and the inconsistencies in the density measurements, it appears that the areal densities in the parts of the separated isotopic samples illuminated by the neutron beam are uncertain by approximately 2%. This is the principal systematic error in the experiment.

The data were analyzed in two ways. In the first method, the individual cross sections σ_i were determined by comparing the sample-in and sample-out count rates. In the second method, the cross section differences $\sigma_{i-j}^{diff}=\sigma_i-\sigma_j$ were determined directly by comparing the count rates for the two samples. Corrections were made for the small differences in the areal densities of the samples using the individual values of σ_i. The second method has the advantage of eliminating the statistical error associated with the sample-out measurement, and it also minimizes possible systematic errors due to count-rate-dependent effects. The data from both analysis methods will be made available via the database maintained by the National Neutron Data Center at the Brookhaven National Laboratory. All of these results will include the normalization required for agreement between the isotopically weighted cross sections and the results from the natural W sample.

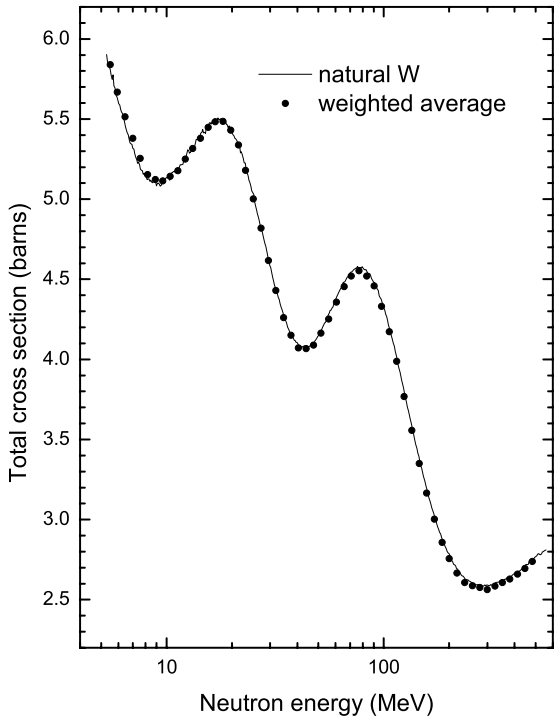

FIG. 1. Comparison of an isotopically weighted combination of the cross sections for the separated tungsten isotopes with the cross section measured for natural tungsten [14].

The cross section difference data are presented as the ratio of the measured difference to the average of the individual cross sections; i.e., as $R_{i-j}=2\sigma_{i-j}^{diff}/(\sigma_i+\sigma_j)$. This has the advantage that the important systematic error due to the densities takes a very simple form. For $R\ll 1$, a condition that is well satisfied for these measurements, it is easily shown that

$$R_{i-j}=2\frac{\sigma_{i-j}^{diff}}{\sigma_i+\sigma_j}\pm 2\frac{\Delta\sigma_{i-j}^{diff}}{\sigma_i+\sigma_j}\pm\frac{\Delta(nl)_i}{(nl)_i}\pm\frac{\Delta(nl)_j}{(nl)_j}. \qquad (1)$$

In this expression, $\Delta\sigma_{i-j}^{diff}$ is the statistical uncertainty in the direct measurement of the cross section difference. The statistical uncertainty in R, which is represented by the second term, is shown explicitly in the figures. The last two terms are the fractional uncertainties in the areal densities of the two samples. They correspond to a shift in the vertical scale in the figures, but are not shown explicitly. Because these terms may be as large as 0.02, we allow the theoretical calculations to be shifted by an amount that does not exceed this value, and indicate the size of the shift. In short, the energy variation of the ratios is well determined, but the zero of the vertical scale is not.

III. RAMSAUER AND CONVENTIONAL SPHERICAL OPTICAL MODELS

The nuclear Ramsauer model [20,21] utilizes the assumption that neutron total cross sections can be represented in terms of the interference between waves which pass through the nucleus and those which go around the nucleus. Unlike the atomic Ramsauer effect, where the low energy results in only one angular momentum value entering in the scattering, the model as applied to the nucleus invokes the assumption that the waves which pass through and go around the nucleus can represent in an average way the partial waves with a large range of angular momentum values. Application of the Ramsauer model to total neutron cross sections has resulted in rather good characterizations of their behavior with mass and energy. This finding is particularly important since the other possible explanation for the structure found in total neutron cross sections would be single-particle resonances. Peaks produced by single-particle resonances have a different dependence on the mass number A than those produced by Ramsauer interference.

Early analyses of total neutron cross sections [21–23] gave results that unambiguously support the Ramsauer interpretation rather than the single-particle interpretation. More recently, a very extensive set of total neutron cross sections up to 560 MeV has become available [14,17]. This dataset has also been found [5–7] to be consistent with the predictions of the Ramsauer model. A particularly impressive result of these analyses is the fact that a fit to better than 3% could be obtained over a wide range of mass and energy with this model.

Although the global fits are very good, it is a particular challenge to fit cross section differences for neighboring and near-neighboring nuclei. A study of neighboring nuclei near $A=140$ [24] has been made with the purpose of inferring the isospin portion of the optical potential. This effort was not completely successful. Although the Ramsauer model gave good fits to the cross sections, two complications interfered with the effort to determine the isovector potential.

The first complication is that the proximity of these nuclei to a closed shell causes changes in the isoscalar portion of the imaginary potential from nucleus to nucleus. The second complication, which is particularly relevant to the present case, is that the change in total cross section produced by adding neutrons to the nucleus is smaller than might be expected from a change in radius using the usual mass dependence $A^{1/3}$. This radius change produces an increase in total cross section, but the increase in $N-Z$ results in a change in the potential that reduces the cross section. Both of these results are also present in calculations using the spherical optical model when conventional geometries are used, as will be shown later.

The Ramsauer model [5,21–23] predicts that the total neutron cross section has the form

$$\sigma_T = 2\pi(R+\lambda\!\!\!^{-})^2(1-\alpha\cos\beta), \tag{2}$$

where σ_T is the total neutron cross section, R the nuclear radius, $\lambda\!\!\!^{-}$ the reduced neutron wavelength, α a parameter between 0 and 1, and β an angle that gives the relative phase between the wave that passes through the nucleus and the wave that goes around it. The parameter α is a measure of the effect of absorption in the nucleus and of the averaging of waves of different orbital angular momenta. A value of 0 for α represents the ''black nucleus'' limit, for which the wave striking the nucleus is completely absorbed. Reduction of α from 1 occurs not only because of absorption but also because the contributions from various angular momentum values are not precisely in phase. The phase angle β is expressed as

$$\beta = cA^{1/3}(\sqrt{a+bE}-\sqrt{E}), \tag{3}$$

where a, which is closely related to the real part of the optical potential, may be decomposed into isoscalar and isovector parts as

$$a = a_0 - \frac{N-Z}{A}a_1. \tag{4}$$

Comparing the total neutron cross sections of adjacent isotopes involves changing R and the neutron number N. Clearly, the form of Eq. (2) shows that an increase in R will enhance the cross section via the geometric factor $(R+\lambda\!\!\!^{-})^2$. The two remaining parameters, α and β, also depend on R, but involve the imaginary optical potential in the damping factor α and the real optical potential in the phase angle β. An increase in N for fixed Z increases the parameter $(N-Z)/A$; this will decrease both V and W. The empirical studies in Refs. [5–7] of the parameters in Eq. (2) show very small (less than approximately 5%) variations of α over the entire periodic table. We therefore neglect changes in α in estimating cross section differences among the tungsten isotopes. This conclusion is confirmed by explicit calculation of the derivatives of α with respect to R and $(N-Z)$. This calculation shows that α should vary by less than 1% over the W isotopes, using guidance from phenomenological optical potentials for the isovector component of the imaginary part. Explicit calculation of the cross section differences using Eq. (2) shows that effects of such small variations in α are indeed negligible. We conclude that the variations of β and R are the most important factors in estimating the cross section differences.

The changes in β arise from variations in both R and $(N-Z)/A$. Taking as independent variables the quantities R and A, we easily find from the above expressions the following relation:

$$\frac{\Delta\sigma_T}{\sigma_T} = \left[\alpha\beta\frac{\sin\beta}{1-\alpha\cos\beta} + \frac{2R}{R+\lambda\!\!\!^{-}}\right]\frac{\Delta R}{R} - \alpha\beta\frac{\sin\beta}{1-\alpha\cos\beta}\,\frac{a_1(Z/A)}{(\sqrt{a+bE}-\sqrt{E})\sqrt{a+bE}}\,\frac{\Delta A}{A}. \tag{5}$$

Expressed in this form, the changes caused by variations in the radius and the potential strength have been grouped into terms multiplying $\Delta R/R$ and $\Delta A/A$. Since α is small (0.095), the factor $1-\alpha\cos\beta$ is approximately 1. The second term in square brackets varies slowly with energy and is

TABLE II. Parameters used in the Ramsauer model calculations shown in Fig. 2. The neutron energy E is in MeV.

Nuclear radius R	$1.382A^{1/3}$ fm
Absorption parameter α	0.095
Phase angle parameter a	35.0 MeV
Phase angle parameter b	0.80
Phase angle parameter c	0.61 $\mathrm{MeV}^{-1/2}$
Isoscalar potential parameter a_0	39.0 MeV
Isovector potential parameter a_1	19.5 MeV

just the quantity corresponding to the increase of the nuclear area with increasing R. The important terms in the cross section difference are then the two terms that depend on $\sin\beta$, which are out of phase with the $\cos\beta$ behavior of the cross section. Note that these two terms are opposite in sign.

Parameters in the calculations based on the above equations are shown in Table II. We have assumed a radius proportional to $A^{1/3}$ and an isovector-to-isoscalar ratio $a_1/a_0 = 0.5$, which is frequently obtained in phenomenological optical model analyses. Most of the parameters were taken from Refs. [6,24]. The cancellation of the radius increase by the isospin term in $\Delta\sigma_T/\sigma_T$ is dramatic, yielding a result that is far too low in amplitude and out of phase with the experimental results, as shown by the solid curve in Fig. 2. However, if we were to assume no isospin dependence, i.e. $a_1 = 0$, then we actually obtain a rather good representation of the data (apart from a small phase mismatch), as shown by the dotted curve in Fig. 2, even though the neglect of isospin is physically incorrect.

The above results are corroborated by calculations employing a spherical optical model, as shown in Fig. 3. These calculations are based on a standard global parametrization,

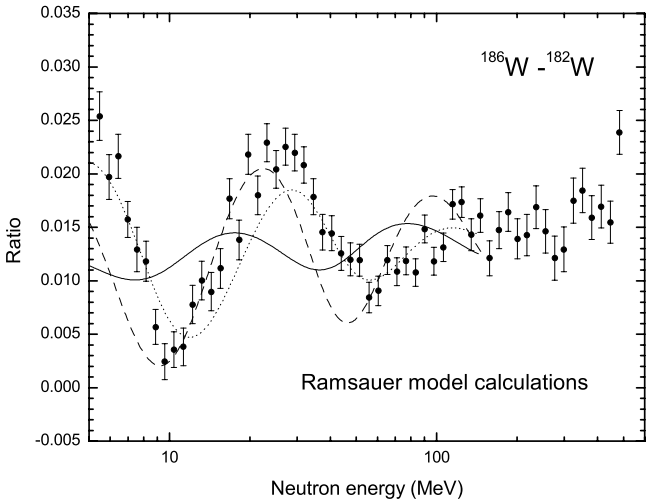

FIG. 2. Results of Ramsauer model calculations compared with measurements for the ^{186}W-^{182}W total cross section difference divided by the average value. The solid line is the full calculation, and the dotted line neglects isospin dependence. The dashed line is a calculation in which the effect of adding neutrons preferentially on the surface has been simulated. No shifts in the vertical scale for the calculations have been made.

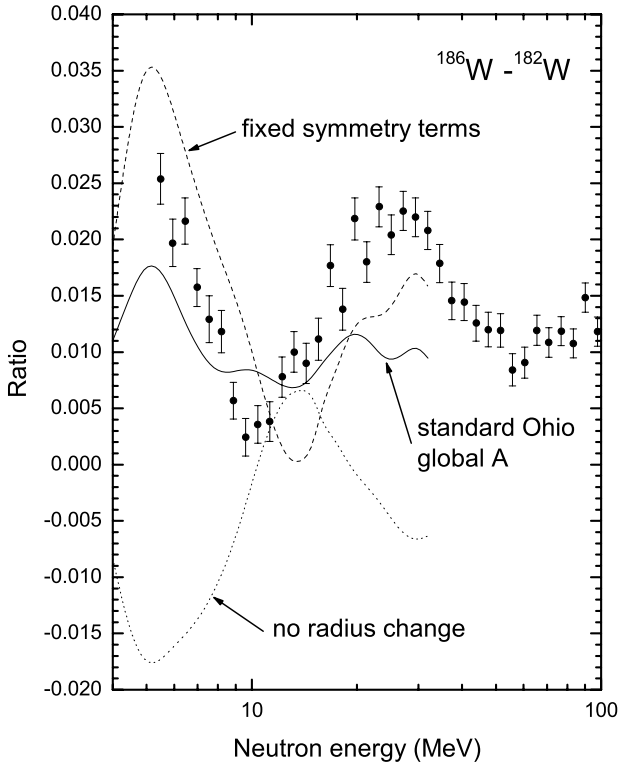

FIG. 3. Spherical optical model calculations for the ^{186}W-^{182}W total cross section difference divided by the average value, compared with the present measurements. The calculations employ the Ohio global A potential [25] (solid curve). The dashed and dotted curves show the effect of omitting the symmetry terms or change in radius, respectively; see text for details. No shifts in the vertical scale for the calculations have been made.

the ''global A'' set from the work of Rapaport, Kulkarni, and Finlay [25]. In this figure, the solid curve, calculated with the unaltered global A potential, yields a very poor reproduction of the experimental data. Fixing the symmetry terms in the optical potential at their value for ^{184}W results in oscillations that resemble the experimental behavior, as shown by the dashed line. On the other hand, using a constant radius (taken as the value for ^{184}W) in all of the calculations yields a result that is large and opposite in phase from that with constant symmetry terms, as shown by the dotted curve.

Since the simplest application of well-known global systematics fails for both the Ramsauer and spherical optical models, we need to consider additional physical ingredients. Specifically, we can investigate the effect of surface modifications of the potential, such as would result from a ''neutron skin.'' A generalization of the Ramsauer model that allows for this possibility has been given in Ref. [26]. The expression that replaces Eq. (2) is

$$\sigma_T = 2\pi(R+\lambda\!\!\!^{-})^2\left[1-\left(1+\frac{2\delta R_n}{R+\lambda\!\!\!^{-}}\right)\alpha\cos\beta+\frac{2\delta R_n}{R+\lambda\!\!\!^{-}}\alpha'\cos\beta'\right], \tag{6}$$

where δR_n is the surface thickness. This version of the model is the equivalent of two square wells and can be used to approximate a neutron skin. Note that the sign of the terms

involving δR_n is opposite from that in Ref. [26], which used a convention that a positive value for δR_n resulted in a decrease in radius. To simulate the effect of adding neutrons preferentially to the surface, we take $\delta R_n = 0$ for ^{182}W and $\delta R_n = 0.28$ fm for ^{186}W. For the present calculations we use a common value for the absorption parameter, i.e. $\alpha = \alpha'$, but decrease the real potential parameter a used to calculate β' to 27 MeV from the value 35 MeV resulting from the parameters a_0 and a_1 shown in Table II. This difference is in the direction we would expect for a neutron interacting with a neutron excess. The result of the calculation is shown by the dashed curve in Fig. 2. Although the agreement is reasonable, it is probably fortuitous because we have added additional parameters. However, it does provide an intuitive argument for expecting that a difference in neutron and proton densities at the surface may be the origin of the observed cross section differences in the W isotopes.

Hartree-Fock calculations give results that do not support the simple assumption that the radius scales as $A^{1/3}$. This is true for relativistic mean-field calculations [27] as well as the Hartree-Fock-Bogoliubov calculations used in Sec. V below. The proton radius tends to stay constant over the tungsten isotopes, while the neutron radius increases from ^{182}W to ^{186}W. The different behavior of the two radii causes some problems with both of the assumptions mentioned previously. The average of the two radii increases more slowly than $A^{1/3}$ over this range. This same feature would tend to change the form factor of the isovector potential over these isotopes. Equivalently, the change can be viewed as a surface layer being added as one moves from ^{182}W to ^{186}W. This changes the constant from that expected if one makes the usual constant-density assumption.

IV. PHENOMENOLOGICAL DISPERSIVE OPTICAL MODEL

In this section we show the results of phenomenological coupled-channel calculations, which take into account the static deformation of the tungsten nuclei. These calculations also incorporate the effects of the dispersion relation connecting the real and imaginary parts of the potential. Even though this treatment is the most detailed of the phenomenological optical models considered here, we will see that the W cross section difference data are still poorly reproduced.

As frequently done in conventional, phenomenological optical model potential (OMP) analyses, each component of the complex, energy-dependent nucleon-nucleus (N-A) potential is described by radial shapes of the Woods-Saxon or derivative Woods-Saxon forms, or by a sum of these two forms. Furthermore, it is assumed that the parameters describing the shapes of these radial functions are independent of energy; only the strength of each term is allowed to vary with energy. This behavior contrasts with that of the semimicroscopic OMP [10,28] where the radial shapes are constructed as energy-dependent functions (see Sec. V).

To incorporate the dispersion-relation effects, we adopt the formalism as described by Mahaux and Sartor [29] for the central component of the optical potential for spherical nuclei, and extend it to the coupled-channel (CC) framework, in which the W isotopes are treated as deformed nuclei. This dispersive CC formalism has proved very successful in recent analyses performed separately for neutrons and protons incident on ^{181}Ta up to 200 MeV [30].

Since the present calculations for W isotopes are closely related to this earlier work on ^{181}Ta, we describe the main features of the n-^{181}Ta potential. Briefly, this CC OMP is local in coordinate space. Its real central component displays two terms. The first one, usually referred to as the Hartree-Fock (HF) potential V_{HF}, is strongest in strength at low incident energy and decreases smoothly with increasing energy. In contrast, the second piece, named as the dispersive term ΔV, is strongly energy dependent. The dispersive term is inferred from those of the surface (W_D) and volume (W_V) components of the imaginary central potential by using dispersion relations. The complete OMP also includes a complex, deformed, and energy-dependent spin-orbit (SO) component.

In contrast to most phenomenological dispersive OMPs that ignore the basic nonlocal character of the underlying N-A effective interaction, here the local dispersive OMP is built following the method outlined by Perey and Buck [31] to obtain an equivalent local potential from a nonlocal one. This method is based on the assumption that nonlocality in coordinate space may be approximated by a Gaussian profile. This approximation is quite successful in spherical OMP analyses as shown by Perey and Buck [31] and more recently by Mahaux and Sartor [29] for extrapolation of the nucleon-nucleus potential from continuum to bound states energies. In our work, the Perey and Buck approximation is used to build the HF potential and calculate the dispersive terms [30]. For the n-^{181}Ta system, the effective ranges of nonlocality were found to be $1.2 \leqslant \beta_{HF} \leqslant 1.4$ fm and $\beta_W \sim 1.2$ fm for the HF and absorptive potentials, respectively. For more details, see Ref. [30].

The full local deformed OMP in the body-fixed system of coordinates has the same functional form for the W isotopes as adopted previously for Ta [30]. It is

$$
\begin{aligned}
-U(\mathbf{r},E) = {} & [V_{HF}(E) + \Delta V_V(E) + iW_V(E)] f_{HF}(\mathbf{r}) \\
& - 4a_D[\Delta V_D(E) + iW_D(E)] \frac{\partial}{\partial r} f_D(\mathbf{r}) \\
& + 2i\lambda_\pi^2 [V_{SO}(E) + iW_{SO}(E)] \nabla f_{SO}(\mathbf{r}) \times \nabla \cdot \mathbf{s},
\end{aligned}
\tag{7}
$$

for incident neutrons. In these expressions, $f_i(\mathbf{r})$, where i is HF, D, or SO, is a deformed Woods-Saxon shape,

$$
f_i(\mathbf{r}) = \left\{ 1 + \exp\left[\frac{r - R_i(\Omega')}{a_i} \right] \right\}^{-1}, \tag{8}
$$

with

$$
R_i(\Omega') = r_i A^{1/3} [1 + \beta_2^i Y_{20}(\Omega') + \beta_4^i Y_{40}(\Omega')], \tag{9}
$$

where β_2^i and β_4^i are quadrupole and hexadecapole deformations, respectively. These deformations are taken in such a way that the deformation lengths

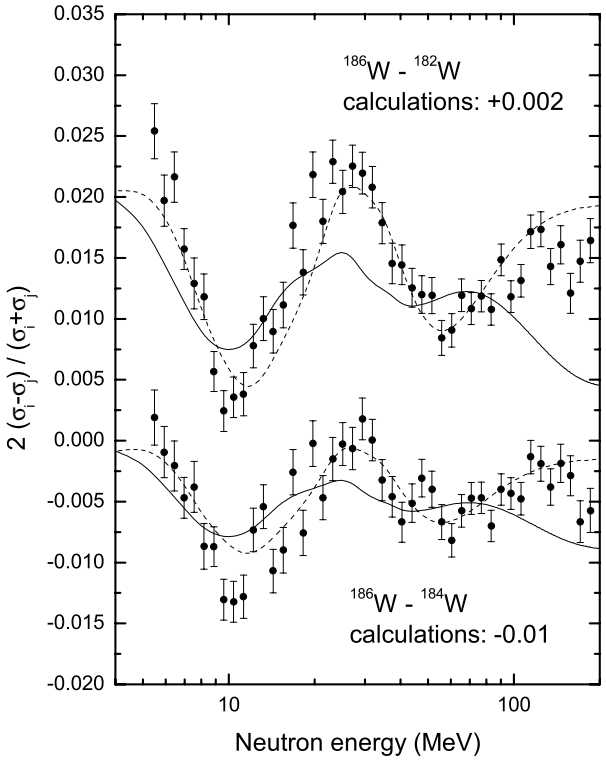

FIG. 4. Results of coupled-channel calculations incorporating dispersion effects compared with measured total cross section differences, plotted as the ratio of the difference to the average of the cross sections. The solid curves include an isovector potential, while the dashed curves do not. The calculations have been shifted by the indicated amounts.

$$\delta_\lambda^i = r_i A^{1/3} \beta_\lambda^i \quad (\lambda = 2,4) \tag{10}$$

are identical for all the OMP components. For more details on energy dependences, geometrical parameters, and deformations, see Ref. [30]. All the CC OMP calculations were performed with the ECIS95 code [32,33] using a rigid rotator model with relativistic kinematics. For ^{181}Ta, the coupling scheme $(7/2^+, 9/2^+, 11/2^+, 13/2^+, 15/2^+)$ was adopted.

The neutron OMP thus defined and tailored to achieve the best overall fit to the available tantalum data includes no explicit separation of the potential into isoscalar and isovector components. The only mass dependence shows up in the potential radii R_i, which we assumed to scale as $A^{1/3}$ in applying the results to the W isotopes. The deformation parameters for the ^{182,184,186}W isotopes were selected by adjusting the deformations β_2 and β_4 so that good fits to published experimental (n,n') scattering data [19,34] are obtained. Within a few percent, these deformations are identical to those published earlier [19,34]. All the CC calculations for W were performed using the coupling basis $(0^+, 2^+, 4^+)$, which is equivalent to that adopted previously for ^{181}Ta.

The CC calculations as described above agree with the measured W total cross sections to within approximately 2% in the range 5–200 MeV, which is reasonable given the uncertainties in sample densities. The total cross section difference calculations, shown by the dashed line, are compared with the present measurements in Fig. 4, where the calculated curves are shifted slightly to optimize the match to the datasets. As can be seen, the magnitude of the oscillations observed in the data when E increases to 200 MeV are rather well reproduced, with only a slight phase mismatch in the case of the ^{186}W-^{182}W difference. This behavior is very similar to that shown for the Ramsauer model (dashed curve in Fig. 2) using the same assumptions: the radius varies as $A^{1/3}$ and the isovector component of the potential is neglected. Thus, as in the Ramsauer calculation, the good agreement is obtained at the expense of an incorrect physical picture.

In a further extension of the coupled-channel analysis with a dispersive optical potential, we have explored the consequences of neglecting isospin. For this purpose we have employed the method suggested by Mahaux and Sartor [35] for making an isoscalar/isovector decomposition of the potential. As a first step we performed a coupled-channel analysis of scattering and reaction data for proton scattering on ^{181}Ta using the same dispersive approach as described above for incident neutrons. This deformed proton OMP was then tested and validated for protons incident on W isotopes by comparison of the predictions with scattering measurements from Refs. [36–39]. Finally, after making the isovector/isoscalar decomposition as in Ref. [35], new neutron potentials were built for the W isotopes and used to calculate the total cross section differences. These results are shown as solid curves in Fig. 4. As can be seen, the results are in significant disagreement with the data, both in the magnitude of the oscillations and the phasing, even though a reasonable treatment of isospin has now been included. These features are similar to those shown in Sec. III.

V. FOLDING OPTICAL MODEL CALCULATIONS

We have performed calculations of the total cross section differences among the W isotopes in the energy range 5–200 MeV using a deformed, semimicroscopic optical model potential (SMOMP) obtained by folding an OMP in nuclear matter (NM) that is energy and density dependent with deformed nuclear densities. This SMOMP is a coupled-channel extension of the spherical, Lane-consistent SMOMP of Ref. [10], which is based on the pioneering work of JLM who calculated the optical potential in nuclear matter using a G-matrix formalism [11,12]. We have supplemented these calculations by carrying out folding-model calculations in the range 100–500 MeV using an empirical effective interaction devised by Kelly and Wallace [40]. The two sets of calculations allow the entire energy range where the total cross section differences have been measured to be compared with calculations based on a realistic description of the neutron and proton density distributions.

The important feature of the Lane-consistent SMOMP of Ref. [10] is the determination of significant energy-dependent renormalizations of the JLM isovector potential depths that allow for the fitting of (p,p), (n,n), and (p,n) scattering using the same NM interaction. These isovector normalizations along with their isoscalar counterparts have been obtained by fitting [10] a large amount of scattering and reaction data for $40 \leqslant A \leqslant 209$ and $E \leqslant 200$ MeV. The NM OMP has the form

$$U_{NM}(\rho,\alpha,E)=\lambda_v(E)[V_0(\rho,E)+\lambda_{v1}(E)\alpha\tau V_1(\rho,E)] + i\lambda_w(E)[W_0(\rho,E)+\lambda_{w1}(E)\alpha\tau W_1(\rho,E)], \tag{11}$$

where $U_{NM}(\rho,\alpha,E)$ is the OMP in NM, ρ is the density of NM, $\alpha=(\rho_n-\rho_p)/(\rho_n+\rho_p)$ is the asymmetry of NM, τ is the isospin of the projectile, V_0, V_1, W_0, and W_1 are the real isoscalar, real isovector, imaginary isoscalar, and imaginary isovector un-renormalized components of the OMP in nuclear matter [11,12,28], respectively, and λ_v, λ_{v1}, λ_w, and λ_{w1} their respective energy-dependent normalization factors [10]. The transition from the NM optical potential to a finite nucleus deformed optical model is performed through a local density approximation (LDA) in a way that is identical to the treatment described in Ref. [41], and includes a downward renormalization of the imaginary potential depths to avoid double counting the inelastic channels explicitly taken into account in the adopted coupling scheme. The following equations show the LDA used in the present folding calculations:

$$U_{r'}(\mathbf{r},E)=(t\sqrt{\pi})^{-3}\int \frac{U_{NM}(\rho(\mathbf{r}'),\alpha(\mathbf{r}'),E)}{\rho(\mathbf{r}')}\rho(\mathbf{r}') \times\exp(-|\mathbf{r}-\mathbf{r}'|^2/t^2)d^3\mathbf{r}', \tag{12}$$

$$U_{r}(\mathbf{r},E)=(t\sqrt{\pi})^{-3}\int \frac{U_{NM}(\rho(\mathbf{r}),\alpha(\mathbf{r}),E)}{\rho(\mathbf{r})}\rho(\mathbf{r}') \times\exp(-|\mathbf{r}-\mathbf{r}'|^2/t^2)d^3\mathbf{r}', \tag{13}$$

$$U(\mathbf{r},E)=0.5[U_{r'}(\mathbf{r},E)+U_r(\mathbf{r},E)]. \tag{14}$$

In Eqs. (12)–(14), $\rho(\mathbf{r})$ is the deformed nuclear density distribution, and t is the range of a Gaussian form factor. The parameter t is taken as 1.25 and 1.35 fm for the real and imaginary OMP components, respectively. $U(\mathbf{r},E)$ is then expressed in a partial wave decomposition suitable for use in coupled-channel calculations: $U(\mathbf{r},E)=\Sigma_l U_l(r,E)\,Y_{l0}(\theta,\phi)$. The present SMOMP also includes a complex deformed spin-orbit potential identical to that described in Ref. [41]. As in Ref. [41], the deformed LDA used in the present study implies a static description of the nuclear deformation. This is appropriate for the deformed W isotopes studied here.

The deformed density distributions used in the present work are calculated in the axially symmetric Hartree-Fock–Bogolyubov framework using the Gogny D1S interaction [8,9]. Salient features of the radial behavior of the monopole components of the HFB densities used in the present calculations are shown in Fig. 5. The rms radius of the neutron distribution is well characterized by $0.926A^{0.34}$, and that for the protons by $2.088A^{0.18}$. The significant deviation of the A dependence of the proton density from the $A^{1/3}$ behavior assumed in global phenomenological optical potentials may explain the success of the calculations described here, in accord with the suggestion based on the Ramsauer analysis. We also note that the rms radius of the neutrons extends beyond

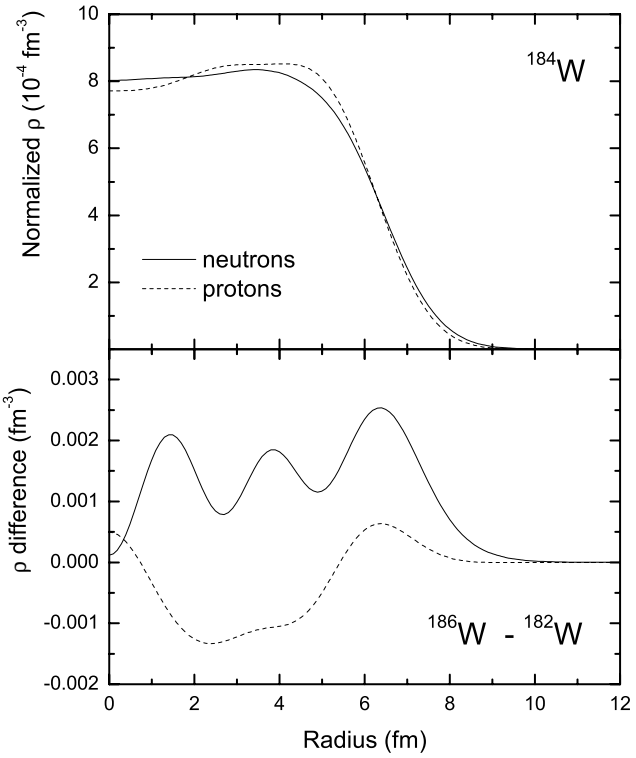

FIG. 5. Monopole component of the HFB densities used in the folding-model calculations. The upper panel shows the neutron and proton densities for ^{184}W, normalized to a single nucleon. The lower panel shows the differences in densities for ^{186}W-^{182}W, for both neutrons and protons.

that for the protons (5.452 fm and 5.339 fm for neutrons and protons in ^{184}W, respectively).

Comparisons of the calculated rms radii as well as the M_{20} and M_{40} moments of the charge densities of the W isotopes with measurements [34,42,43] are presented in Fig. 6. These comparisons show that the rms charge radii as well as the charge M_{20} moments are well described by the HFB calculations. Both the experimental and the calculated radii exhibit an A dependence that is weaker than the usual $A^{1/3}$ dependence (solid line) and is close to an $A^{1/6}$ dependence (dotted line). The M_{40} charge moments are not as well reproduced for ^{182}W and ^{184}W. However, the comparison (see below) between the multipole moments of the different (SMOMP and dispersive phenomenological) optical model potentials seems to argue in favor of the HFB calculations since the phenomenologically fine tuned hexadecapole moments of the DOMP exhibit the same trend as those calculated from the SMOMP using HFB densities.

By inserting the deformed SMOMP into the coupled equations for scattering off the first levels of the ground state rotational band (coupling scheme: 0^+, 2^+, 4^+, 6^+), and solving them using ECIS [32,33] we can accurately account for the differential (n,n') scattering cross sections off ^{182}W [44]. The total cross sections are also reasonably well accounted for; the difference between calculated and measured σ_T stay mostly below the 5% level over the range 5–200 MeV, as can be seen in Fig. 7 for the case of ^{184}W. These calculations yield a quite reasonable reproduction of the W

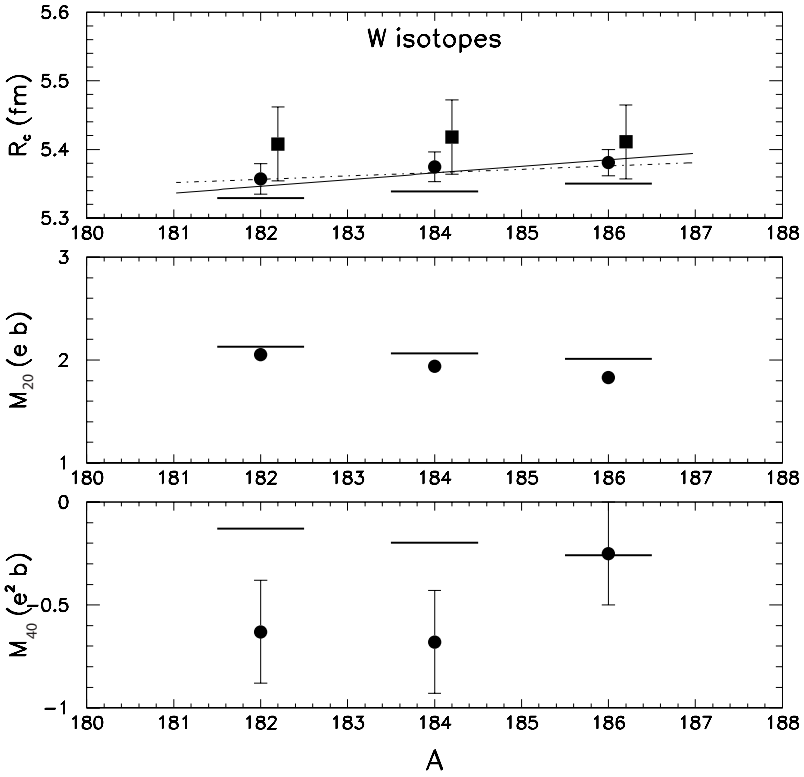

FIG. 6. Comparison between measured and calculated charge rms radii, and quadrupole and hexadecapole moments for W isotopes. The symbols with error bars are the measurements taken from Refs. [34,42,43]. The horizontal bars are results of the HFB calculations used in the present work. The solid and dotted lines in the top panel represent $A^{1/3}$ and $A^{1/6}$ dependences, respectively.

isotope total cross section differences, as shown by the solid curves in Fig. 8. The general behavior of both the amplitude and the phase of the energy variations is rather well reproduced by the calculations. This is a significant improvement over the models described earlier that do not utilize a realistic description of the variation in neutron and proton densities over the isotopic chain. The calculated amplitude of the energy variations is slightly lower than observed experimentally. This feature is most probably associated with the behavior of the total cross section as seen in Fig. 7, since here also the oscillations in the calculated cross sections are lower than seen in the measurements. Such behavior is not specific to the W region, since it is a systematic feature of all JLM calculations in heavy nuclei [10,14,28].

The improvement shown by the SMOMP calculations raises the following question: can this improvement be traced to one of the features of the SMOMP, or put in another way, which one of the differences between the SMOMP and the other models leads to the improvement observed here? We will first assess the importance of solving the neutron scattering problem in the coupled-channel framework, versus a spherical OMP approach. This was achieved by comparing the result of the SMOMP calculation as described above with the result of using the SMOMP potential in a spherical framework. This comparison, shown by the short-dashed lines in Fig. 8, indicates that the W total cross section differences studied here do not exhibit a strong sensitivity to the treatment (spherical or coupled channels) above a few MeV. At the lowest energies the coupled-channel treatment is superior. However, one must remember that the ^{182,184,186}W isotopes, since they have a quadrupole deformation $\beta_2 \approx 0.26$, ought to be treated in the coupled-channel framework in order to account for the non-negligible inelastic scattering to the easily excited states of the ground state rotational band.

The spin-orbit component of the SMOMP can also be eliminated as the reason for the improved agreement of the

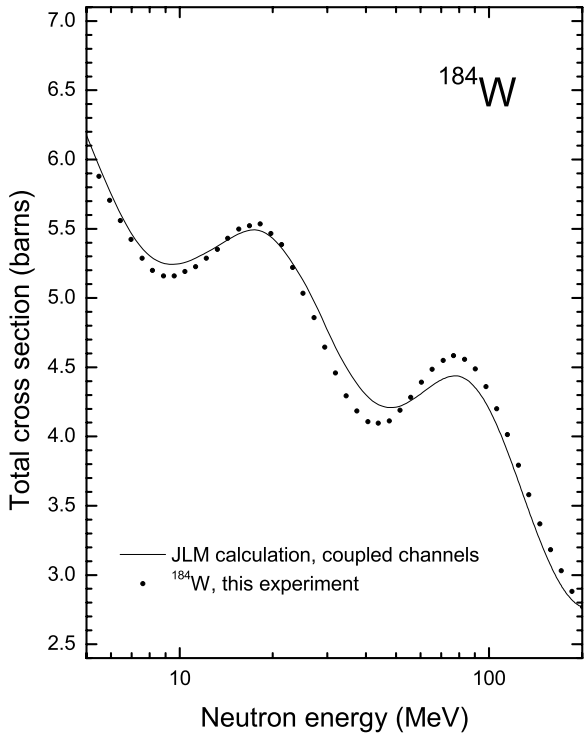

FIG. 7. Total cross section for $n+{}^{184}$W. The dots represent our measurement, and the line shows the results of the semimicroscopic folding-model calculation described in Sec. V.

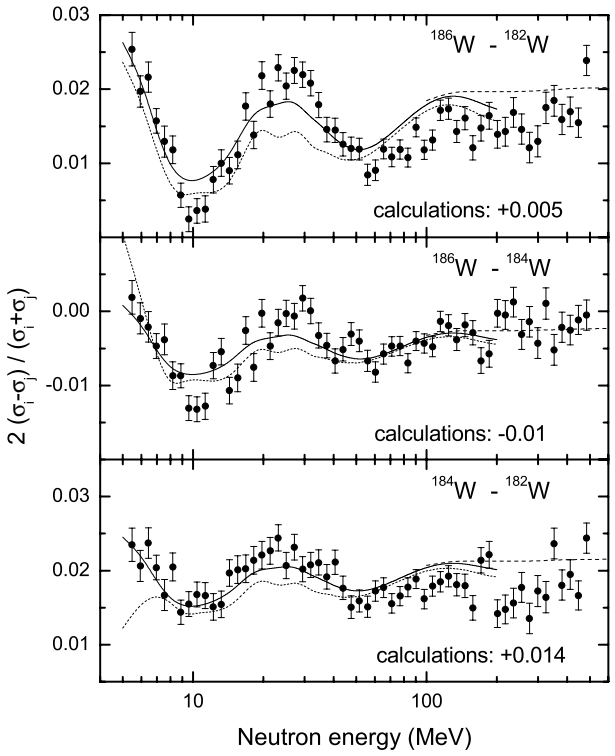

FIG. 8. Comparison between folding optical model calculations based on HFB densities and measured W total cross section differences, represented as the ratio of the difference to the average cross section. The solid curves are JLM coupled-channel calculations, and the short-dashed curves are corresponding spherical calculations. The long-dashed curves above 100 MeV are EEI calculations. The calculations are shifted by the specified amounts, which are smaller than the uncertainties associated with sample densities (see Sec. II).

SMOMP with the W total cross section differences. We checked that changes of the spin-orbit terms do not affect the total cross section in a significant way.

Similarly, the detailed structure of the nuclear density distribution does not seem to play an essential role in accounting for the total cross section differences among the W isotopes. A SMOMP calculation performed using a Woods-Saxon density fitted to the monopole component of the HFB results (preserving *A*, *Z*, and the neutron and proton rms radii) gives very similar results to the full SMOMP calculation using HFB densities. This result strongly indicates that the change in the behavior of the neutron and proton rms radii across the isotopic chain is the principal ingredient in the HFB calculations, which yields favorable results for the cross section differences.

In order to evaluate the influence of the energy dependence of the potential depths, a SMOMP calculation was performed using energy-independent potential depth normalization factors fixed at the average values of the energy-dependent ones. Below 60 MeV, this calculation does not exhibit significant differences with the full-fledged SMOMP calculation showing that the success of the SMOMP cannot be fully attributed to the detailed energy dependence of the potential depths. However, above 60 MeV, the calculation performed with the energy-independent normalization factors seems to overpredict the amplitude of the variations of W σ_T differences compared to that of the experimental data or that of the energy-dependent calculation results. Thus, although it does not explain the quality of the SMOMP prediction over the full 5–200 MeV energy range, the energy dependence of the SMOMP plays an important role, especially at higher energies.

To extend the folding-model treatment of the cross section differences to high energies, we have also performed calculations in the 100–500 MeV range using the empirical effective interaction (EEI) developed by Kelly and Wallace [40]. This interaction, originally developed at six discrete energies in the 135–650 MeV range, was interpolated in energy and used in Ref. [14] to interpret neutron total cross section data. The reproduction of the experimental results was very good, and it was also found that proton reaction cross sections were well reproduced. As is the case for the JLM-based calculations described above, the EEI is density dependent and is applied in finite nuclei using a local density approximation. Details of the calculations may be found in Ref. [14]. The densities employed in the EEI calculations were the same HFB densities used in the JLM calculations. The results are shown by the long-dashed lines in Fig. 8. These calculations exhibit very little energy dependence, in agreement with experiment. There is reasonable agreement between the JLM and EEI calculations in the region of overlap between 100 and 200 MeV.

VI. CONCLUSIONS

The total cross sections of the tungsten isotopes are perplexing. Whereas other isotopic data, such as ^{142}Ce-^{140}Ce can be more easily fit with spherical optical model calculations that include reasonable strengths for the isospin potential, the tungsten data are not amenable to such simple calculations. We have demonstrated using the simple Ramsauer model that the most likely source of the cross section differences is the nuclear surface. We have shown that the extended (deformed) optical model gives essentially the same results as the Ramsauer and spherical models when isospin is properly incorporated, and thus cannot explain the measured isotopic differences. We have also shown that a folding model based on Hartree-Fock wave functions, when used with a Lane-consistent effective interaction, can reasonably accurately fit the results of the measurements. An examination of the proton and neutron densities from the Hartree-Fock calculation indeed shows a neutron distribution that extends somewhat beyond that of the protons, in qualitative agreement with the conclusions drawn from the Ramsauer model.

In summary, we have shown for the first time that although standard phenomenological optical models are capable of predicting neutron total cross sections at the few percent level, the more complicated folding model is required to achieve a detailed explanation of total cross section differences among neighboring nuclei. This result is a consequence of the realistic treatment of the separate proton and neutron densities, which is possible in such a model.

ACKNOWLEDGMENTS

We would like to thank Dr. L. S. Waters and the Accelerator Production of Tritium Project (APT) for sponsoring the measurements of which the present work was a part. The theoretical interpretation of the measurements was conducted under the auspices of an agreement between CEA/DAM and NNSA/DP on cooperation in fundamental science. This work was performed under the auspices of the U.S. Department of Energy by the University of California, Lawrence Livermore National Laboratory under Contract No. W-7405-Eng-48, the Los Alamos National Laboratory under Contract No. W-7405-Eng-36, and by Ohio University under Contract No. DE-FG02-88ER40387.

[1] H.S. Camarda, T.W. Phillips, and R.M. White, Phys. Rev. C **29**, 2106 (1984).
[2] R.E. Shamu, E.M. Bernstein, J.J. Ramirez, and Ch. Lagrange, Phys. Rev. C **22**, 1857 (1980).
[3] F.S. Dietrich (unpublished).
[4] H.S. Camarda, F.S. Dietrich, and T.W. Phillips, Phys. Rev. C **39**, 1725 (1986).
[5] S.M. Grimes, J.D. Anderson, R.W. Bauer, and V.A. Madsen, Nucl. Sci. Eng. **130**, 340 (1998).
[6] R.W. Bauer, J.D. Anderson, S.M. Grimes, D.A. Knapp, and V.A. Madsen, Nucl. Sci. Eng. **130**, 348 (1998).
[7] S.M. Grimes, J.D. Anderson, R.W. Bauer, and V.A. Madsen, Nucl. Sci. Eng. **134**, 77 (2000).
[8] J. Dechargé and D. Gogny, Phys. Rev. C **21**, 1568 (1980).
[9] J.-F. Berger, M. Girod, and D. Gogny, Comput. Phys. Commun. **63**, 365 (1990).
[10] E. Bauge, J.-P. Delaroche, and M. Girod, Phys. Rev. C **63**, 024607 (2001).
[11] J.-P. Jeukenne, A. Lejeune, and C. Mahaux, Phys. Rev. C **15**, 10 (1977).
[12] J.-P. Jeukenne, A. Lejeune, and C. Mahaux, Phys. Rev. C **16**, 80 (1977).
[13] A.M. Lane, Nucl. Phys. **35**, 676 (1962).
[14] W.P. Abfalterer, F.B. Bateman, F.S. Dietrich, R.W. Finlay, R.C. Haight, and G.L. Morgan, Phys. Rev. C **63**, 044608 (2001).
[15] W.P. Abfalterer *et al.*, Phys. Rev. Lett. **81**, 57 (1998).
[16] W.P. Abfalterer, F.B. Bateman, F.S. Dietrich, R.W. Finlay, R.C. Haight, and G.L. Morgan, Los Alamos National Laboratory Report No. LA-UR-99-666, 1999.
[17] R.W. Finlay, W.P. Abfalterer, G. Fink, E. Montei, T. Adami, P.W. Lisowski, G.L. Morgan, and R.C. Haight, Phys. Rev. C **47**, 237 (1993).
[18] P.T. Guenther, A.B. Smith, and J.F. Whalen, Phys. Rev. C **26**, 2433 (1982).
[19] J.R.M. Annand and R.W. Finlay, Nucl. Phys. **A442**, 234 (1985).
[20] J.D. Lawson, Philos. Mag. **44**, 102 (1953).
[21] J.M. Peterson, Phys. Rev. **125**, 925 (1962).
[22] V. Franco, Phys. Rev. **140**, B1501 (1965).
[23] K.W. McVoy, Ann. Phys. (N.Y.) **43**, 91 (1967).
[24] J.D. Anderson and S.M. Grimes, Phys. Rev. C **41**, 2904 (1990).
[25] J. Rapaport, V. Kulkarni, and R.W. Finlay, Nucl. Phys. **A330**, 15 (1979).
[26] V.A. Madsen, J.D. Anderson, S.M. Grimes, V.R. Brown, and P.M. Anthony, Phys. Rev. C **56**, 365 (1997).
[27] G.A. Lalazissis, S. Raman, and P. Ring, At. Data Nucl. Data Tables **71**, 1 (1999).
[28] E. Bauge, J.-P. Delaroche, and M. Girod, Phys. Rev. C **58**, 1118 (1998).
[29] C. Mahaux and R. Sartor, Adv. Nucl. Phys. **20**, 1 (1991).
[30] P. Romain and J.-P. Delaroche, *Proceedings of a Specialists' Meeting on the Nucleon Nucleus Optical Model up to 200 MeV, Bruyères-le-Châtel, France, 1996* (OECD, Paris, France, 1997); see http://db.nea.fr/html/science/om200/, p. 167.
[31] F. Perey and B. Buck, Nucl. Phys. **32**, 353 (1962).
[32] J. Raynal, computer code ECIS (unpublished).
[33] J. Raynal, Commissariat à l'Energie Atomique Report No. CEA-N-2772, 1994.
[34] J.-P. Delaroche, G. Haouat, J. Lachkar, Y. Patin, J. Sigaud, and J. Chardine, Phys. Rev. C **23**, 136 (1981).
[35] C. Mahaux and R. Sartor, Nucl. Phys. **A481**, 407 (1988).
[36] T. Kruse, W. Makofske, H. Ogata, W. Savin, M. Slagowitz, and M. Williams, Nucl. Phys. **A169**, 177 (1971).
[37] T. Ichihara, H. Sakagushi, M. Nakamura, M. Yosoi, M. Iteri, Y. Takeuchi, H. Togawa, T. Tsutsumi, and S. Kobayashi, Phys. Lett. B **182**, 301 (1986).
[38] T. Ichihara, H. Sakagushi, M. Nakamura, M. Yosoi, M. Iteri, Y. Takeuchi, H. Togawa, T. Tsutsumi, and S. Kobayashi, Phys. Rev. C **36**, 1754 (1987).
[39] B.G. Lay, S.M. Banks, B.M. Spicer, G.G. Shute, V.C. Officer, R.M. Ronningen, G.M. Crawley, N. Anantaraman, and R.P. DeVito, Phys. Rev. C **32**, 440 (1985).
[40] J.J. Kelly and S.J. Wallace, Phys. Rev. C **49**, 1315 (1994).
[41] E. Bauge, J.-P. Delaroche, M. Girod, G. Haouat, J. Lachkar, Y. Patin, J. Sigaud, and J. Chardine, Phys. Rev. C **61**, 034306 (2000).
[42] E.G. Nadjakov, K.P. Marinova, and Y.P. Gangrsky, At. Data Nucl. Data Tables **56**, 133 (1994).
[43] I.Y. Lee *et al.*, Phys. Rev. C **12**, 1483 (1975).
[44] E. Bauge, J.-P. Delaroche, and M. Girod, Nucl. Phys. **A654**, 829c (1999).